


Reexamination of the rare decay $B_s \rightarrow \phi\mu^+\mu^-$ using holographic light-front QCD

Mohammad Ahmady^{✉,*}, Spencer Keller^{✉,†} and Michael Thibodeau^{✉,‡}

Department of Physics, Mount Allison University, Sackville, New Brunswick E4L 1E6, Canada

Ruben Sandapen^{✉,§}

*Department of Physics, Acadia University, Wolfville, Nova-Scotia B4P 2R6, Canada
and Department of Physics, Mount Allison University, Sackville,
New Brunswick E4L 1E6, Canada*

 (Received 17 October 2019; published 13 December 2019)

We calculate the Standard Model (SM) predictions for the differential branching ratio of the rare $B_s \rightarrow \phi\mu^+\mu^-$ decays using $B_s \rightarrow \phi$ transition form factors (TFFs) obtained using holographic light-front QCD (hQCD) instead of the traditional QCD sum rules (QCDSR). Our predictions for the differential branching ratio is in better agreement with the LHCb data. Also, we find that the hQCD prediction for $R_{K^*\phi}$, the ratio of the branching fraction of $B \rightarrow K^*\mu^+\mu^-$ to that of $B_s \rightarrow \phi\mu^+\mu^-$, is in excellent agreement with both the LHCb and CDF results in low q^2 range.

DOI: [10.1103/PhysRevD.100.113005](https://doi.org/10.1103/PhysRevD.100.113005)

I. INTRODUCTION

The flavor changing neutral current (FCNC) $b \rightarrow s$ transition, which is forbidden at tree-level, has been at the focus of extensive experimental and theoretical investigations. This is due to the fact that, among other things, this rare transition is sensitive to new physics (NP), i.e., physics beyond the Standard Model (SM). In extensions of the SM, new heavy particles can appear in competing diagrams and affect both the branching fraction of the decay and the angular distributions of the final-state particles. In particular, the semileptonic $b \rightarrow s\ell^+\ell^-$ quark decay has received significant attention via measurements of inclusive $B \rightarrow X_s\ell^+\ell^-$ and exclusive $B \rightarrow K\mu^+\mu^-$ and $B \rightarrow K^*\mu^+\mu^-$ decays and their comparison against the SM predictions. Many observables for the dileptonic $B \rightarrow K^*\mu^+\mu^-$ decay have already been measured and the precision of the experimental data is expected to improve significantly in the near future. The decay $B_s \rightarrow \phi\mu^+\mu^-$, which is closely related to the decay $B \rightarrow K^*\mu^+\mu^-$, provides an alternate venue to examine the same underlying

quark process, as shown in Fig. 1, in a different hadronic environment. This decay channel was first observed and studied by the CDF collaboration [1,2] and subsequently studied by the LHCb collaboration using data collected during 2011, corresponding to an integrated luminosity of 1.0 fb^{-1} [3]. Although B_s meson production is suppressed with respect to the B_d meson by the fragmentation fraction ratio $f_s/f_d \sim 1/4$, the narrow ϕ resonance allows a clean selection with low background levels. While the angular distributions were found to be in good agreement with SM expectations, the measured branching fraction deviates from the recently updated SM prediction by 3.1σ [4–7]:

$$\begin{aligned} & \frac{d}{dq^2} \text{BR}(B_s \rightarrow \phi\mu^+\mu^-)|_{q^2 \in [1:6] \text{ GeV}^2} \\ &= \begin{cases} (2.58_{-0.31}^{+0.33} \pm 0.08 \pm 0.19) \times 10^{-8} \text{ GeV}^{-2} & (\text{exp}) \\ (4.81 \pm 0.56) \times 10^{-8} \text{ GeV}^{-2} & (\text{SM}), \end{cases} \end{aligned} \quad (1)$$

where $q^2 = m_{\mu\mu}^2$ is the invariant mass of the produced dimuons. A similar trend is also seen for the branching fractions of other $b \rightarrow s\mu^+\mu^-$ processes, which tend to be lower than the SM predictions [8–10].

One important aspect of SM theoretical predictions of the exclusive decays is the computation of the transition form factors (TFFs) which parametrize the hadronic matrix elements of $B_{(s)}$ to light mesons through quark currents. These nonperturbative TFFs are commonly evaluated using light-cone sum rules (LCSR) [11] with the input distribution

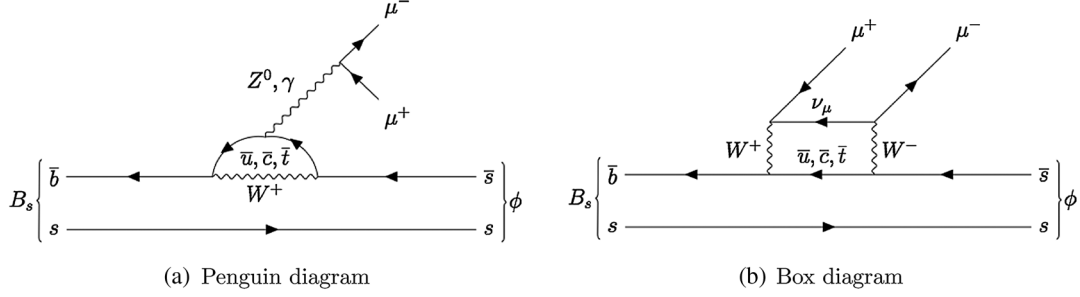
* mahmady@mta.ca

† stkeller@mta.ca

‡ methibodeau@mta.ca

§ ruben.sandapen@acadiau.ca

Published by the American Physical Society under the terms of the Creative Commons Attribution 4.0 International license. Further distribution of this work must maintain attribution to the author(s) and the published article's title, journal citation, and DOI. Funded by SCOAP³.


 FIG. 1. Feynman diagrams of the principal contributions to the $B_s \rightarrow \phi \mu^+ \mu^-$ decay.

amplitudes (DAs) obtained via the traditional QCD sum rules (QCDSR). An alternative is to calculate these DAs using the light-front wave function of the light meson bound state. In a recent work, we have shown that the light-front wave functions for ρ and ϕ mesons resulting from holographic light-front QCD (hQCD) leads to predictions for diffractive production cross sections of these vector mesons that are in good agreement with the experimental data [12]. This is our motivation to use the hQCD DAs to calculate the $B_s \rightarrow \phi$ TFFs and consequently, provide alternative predictions for the $B_s \rightarrow \phi \mu^+ \mu^-$ differential branching ratio. The nonperturbative TFFs are the dominant source of the theoretical uncertainty in this decay mode and therefore it is important to improve our understanding of the corresponding error by examining viable models.

II. HOLOGRAPHIC MESON WAVEFUNCTIONS

In recent years, new insights about hadronic light-front wave functions based on the anti-de Sitter/conformal field theory (AdS/CFT) correspondence have been proposed by Brodsky and de Téramond [13–15]. In a semiclassical approximation of light-front QCD where quark masses and quantum loops are neglected, the meson wave function can be written as [16]

$$\Psi(x, \zeta, \phi) = e^{iL\phi} \mathcal{X}(x) \frac{\phi(\zeta)}{\sqrt{2\pi\zeta}} \quad (2)$$

where the variable $\zeta = \sqrt{x(1-x)}r$ is the transverse separation between the quark and the antiquark at equal light-front time. The transverse wave function $\phi(\zeta)$ is a solution of the so-called holographic light-front Schrödinger equation:

$$\left(-\frac{d^2}{d\zeta^2} - \frac{1-4L^2}{4\zeta^2} + U(\zeta) \right) \phi(\zeta) = M^2 \phi(\zeta) \quad (3)$$

where M is the mass of the meson and $U(\zeta)$ is the confining potential which at present cannot be computed from first-principles in QCD. On the other hand, making the substitutions $\zeta \rightarrow z$ where z being the fifth dimension of AdS space, together with $L^2 - (2-J)^2 \rightarrow (mR)^2$ where R and

m are the radius of curvature and mass parameter of AdS space respectively, Eq. (3) describes the propagation of spin- J string modes in 5-D AdS space. In this case, the potential is given by

$$U(z, J) = \frac{1}{2} \varphi''(z) + \frac{1}{4} \varphi'(z)^2 + \left(\frac{2J-3}{4z} \right) \varphi'(z) \quad (4)$$

where $\varphi(z)$ is the dilaton field which breaks the conformal invariance of AdS space. A quadratic dilaton ($\varphi(z) = \kappa^2 z^2$) profile results in a harmonic oscillator potential in physical spacetime:

$$U(\zeta, J) = \kappa^4 \zeta^2 + \kappa^2 (J-1). \quad (5)$$

The choice of a quadratic dilaton is dictated by the de Alfaro, Fubini and Furlan (dAFF) [17] mechanism for breaking conformal symmetry in the Hamiltonian while retaining the conformal invariance of the action [18]. Solving the holographic Schrödinger equation with this harmonic potential given by Eq. (5) yields the meson mass spectrum,

$$M^2 = 4\kappa^2 \left(n + L + \frac{S}{2} \right) \quad (6)$$

with the corresponding normalized eigenfunctions

$$\phi_{n,L}(\zeta) = \kappa^{1+L} \sqrt{\frac{2n!}{(n+L)!}} \zeta^{1/2+L} \exp\left(\frac{-\kappa^2 \zeta^2}{2}\right) L_n^L(x^2 \zeta^2). \quad (7)$$

To completely specify the holographic wave function given by Eq. (2), the longitudinal wavefunction $\mathcal{X}(x)$ must be determined. For massless quarks, this is achieved by an exact mapping of the pion electromagnetic form factors in AdS and in physical spacetime resulting in [16].

$$\mathcal{X}(x) = \sqrt{x(1-x)}. \quad (8)$$

Equation (6) predicts that the mesons lie on linear Regge trajectories as is experimentally observed and thus κ can be

chosen to fit the Regge slope. Reference [16] reports $\kappa = 0.54$ GeV for vector mesons. Equation (6) also predicts that the pion and kaon (with $n = 0, L = 0, S = 0$) are massless. For the ground state mesons with $n = 0, L = 0$, Eq. (2) becomes

$$\Psi(x, \zeta) = \frac{\kappa}{\sqrt{\pi}} \sqrt{x(1-x)} \exp\left[-\frac{\kappa^2 \zeta^2}{2}\right]. \quad (9)$$

To account for nonzero quark masses, we follow the prescription of Brodsky and de Téramond given in Ref. [19] which leads to an augmented form for the transverse part of the light-front wave function:

$$\Psi_\lambda^\phi(x, \zeta) = \mathcal{N}_\lambda \sqrt{x(1-x)} \exp\left[-\frac{\kappa^2 \zeta^2}{2}\right] \times \exp\left[-\frac{m_s^2}{2\kappa^2 x(1-x)}\right], \quad (10)$$

where we have introduced a polarization-dependent normalization constant \mathcal{N}_λ where $\lambda = L, T$. Including the spin structure, the vector meson light-front wave functions can be written as [20]

$$\Psi_{h,\bar{h}}^{\phi,L}(x, r) = \frac{1}{2} \delta_{h,-\bar{h}} \left[1 + \frac{m_s^2 - \nabla_r^2}{x(1-x)M_V^2}\right] \Psi_L^\phi(x, \zeta), \quad (11)$$

and

$$\Psi_{h,\bar{h}}^{\phi,T}(x, r) = \pm \left[ie^{\pm i\theta_r} (x\delta_{h\pm, \bar{h}\mp} - (1-x)\delta_{h\mp, \bar{h}\pm}) \partial_r + m_s \delta_{h\pm, \bar{h}\pm}\right] \frac{\Psi_T^\phi(x, \zeta)}{2x(1-x)}. \quad (12)$$

We fix the normalization constant \mathcal{N}_λ in Eq. (10) by requiring that

$$\sum_{h,\bar{h}} \int d^2\mathbf{r} dx |\Psi_{h,\bar{h}}^{\phi,\lambda}(x, r)|^2 = 1. \quad (13)$$

Previously, we have used holographic light-front wave functions to calculate hadronic effects in rare B decays to ρ and ϕ [21–26].

III. DECAY CONSTANTS AND DISTRIBUTION AMPLITUDES

Having specified the holographic wave function for ϕ meson, we are now able to predict their vector and tensor couplings, f_ϕ and f_ϕ^T respectively, defined by [27]

$$\langle 0|\bar{s}(0)\gamma^\mu s(0)|\phi(P, \lambda)\rangle = f_\phi M_\phi e_\lambda^\mu \quad (14)$$

and

TABLE I. Our predictions for the longitudinal and transverse decay constants and their ratio for the ϕ meson using $\kappa = 0.54 \pm 0.02$ GeV and $m_s = 0.40 \pm 0.15$ GeV.

| Reference | Approach | f_ϕ [MeV] | f_ϕ^\perp [MeV] | f_ϕ^\perp/f_ϕ |
|------------|----------------------|-------------------|-------------------------|-----------------------|
| This paper | LF holography | 190 ± 20 | 150_{-20}^{+10} | 0.79 ± 0.13 |
| PDG [28] | Exp. data | 225 ± 2 | | |
| Ref. [30] | Sum Rules | 254 ± 3 | 204 ± 14 | |
| Ref. [31] | Lattice (continuum) | | | 0.76 ± 0.01 |
| Ref. [32] | Lattice (finite) | | | 0.780 ± 0.008 |
| Ref. [33] | Lattice (unquenched) | | | |
| Ref. [34] | Dyson-Schwinger | 190 | 150 | 0.79 |

$$\langle 0|\bar{s}(0)[\gamma^\mu, \gamma^\nu]s(0)|\phi(P, \lambda)\rangle = 2f_\phi^T(e_\lambda^\mu P^\nu - e_\lambda^\nu P^\mu), \quad (15)$$

respectively. In Eqs. (14) and (15), the strange quark and antiquark fields evaluated at the same spacetime point, P^μ and e_λ^μ are the momentum and polarization vectors of the ϕ meson. It follows that [12,26]

$$f_\phi = \sqrt{\frac{N_c}{\pi}} \int_0^1 dx \left[1 + \frac{m_s^2 - \nabla_r^2}{x(1-x)M_V^2}\right] \Psi_L^\phi(x, \zeta)|_{r=0} \quad (16)$$

and

$$f_\phi^\perp(\mu) = \sqrt{\frac{N_c}{2\pi}} m_s \int_0^1 dx \int d\mathbf{r} \mu J_1(\mu r) \frac{\Psi_T^\phi(x, \zeta)}{x(1-x)} \quad (17)$$

respectively. The vector coupling is also referred to as the decay constant as it is related to the measured electronic decay width $\Gamma_{V \rightarrow e^+e^-}$ of the vector meson:

$$\Gamma_{\phi \rightarrow e^+e^-} = \frac{4\pi\alpha_{em}^2}{27M_\phi} f_\phi^2. \quad (18)$$

Using the experimental measurement $\Gamma_{\phi \rightarrow e^+e^-} = 1.263 \pm 0.15$ KeV [28], and the running of the fine structure constant below 1 GeV [29], we obtain $f_\phi = 225 \pm 2$ MeV. In Table I, we compare our predictions for the decay constants with those obtained from lattice QCD and other hadronic models as well as the available experimental data. We note that we underestimate the electronic decay width due to the fact that there are likely perturbative corrections that must be taken into account when predicting the electronic decay width.

IV. DISTRIBUTION AMPLITUDES FOR THE ϕ

We now proceed to predict the twist-2 DAs $\phi_{K^*}^{\parallel, \perp}(x, \mu)$ given by [25]:

$$f_\phi \phi_\parallel(x, \mu) = \sqrt{\frac{N_c}{\pi}} \int db \mu J_1(\mu b) \left[1 + \frac{m_s^2 - \nabla_b^2}{M_\phi^2 x(1-x)}\right] \times \frac{\Psi_L^\phi(x, \zeta)}{x(1-x)}, \quad (19)$$

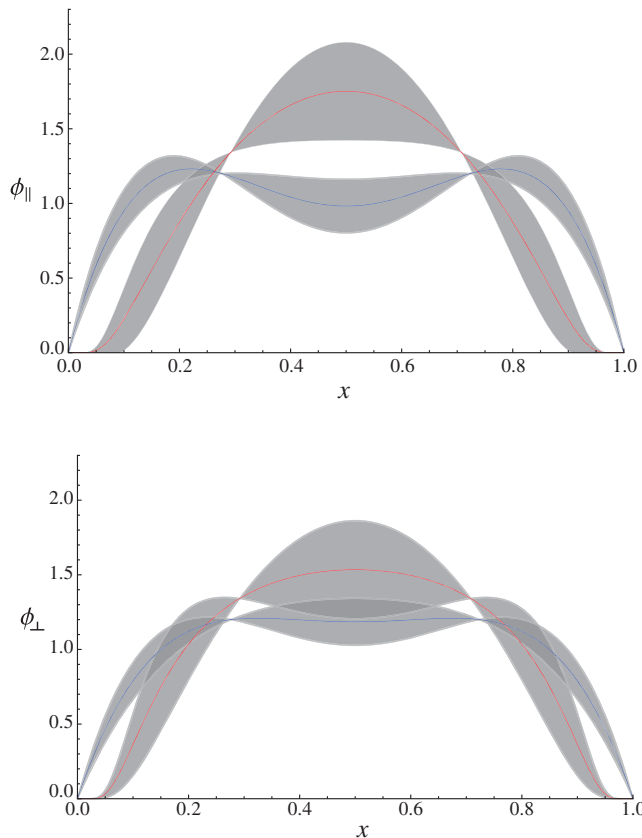


FIG. 2. Twist-2 DAs predicted by hQCD (red curve) and SR (blue curve). The uncertainty band is due to the variation of the quark mass and the fundamental scale for holographic QCD and the error bar on Gegenbauer coefficients for SR.

and

$$f_{\phi}^{\perp}(\mu)\phi_{\perp}(x,\mu) = m_s \sqrt{\frac{N_c}{2\pi}} \int db \mu J_1(\mu b) \frac{\Psi_T^{\phi}(x,\zeta)}{x(1-x)}. \quad (20)$$

Note that the decay constants are defined in Eqs. (16) and (17) so that the twist-2 DAs satisfy the normalization condition, i.e.,

$$\int \phi_{\parallel,\perp}(x,\mu) dx = 1. \quad (21)$$

We can now compare the holographic DAs with those obtained using QCDSR. QCDSR predict the moments of the DAs:

$$\langle \xi_{\parallel,\perp}^n \rangle_{\mu} = \int dx \xi^n \phi_{\parallel,\perp}(x,\mu) \quad (22)$$

and that only the first two moments are available in the standard SR approach [35]. The twist-2 DA are then reconstructed as a Gegenbauer expansion

$$\phi_{\parallel,\perp}(x,\mu) = 6x\bar{x} \left\{ 1 + \sum_{j=1}^2 a_j^{\parallel,\perp}(\mu) C_j^{3/2}(2x-1) \right\}, \quad (23)$$

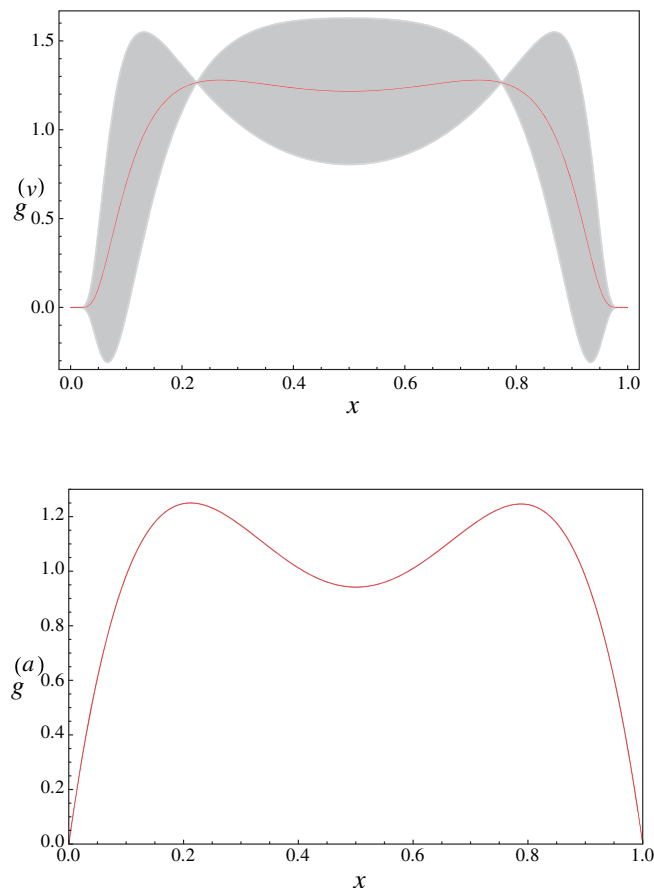


FIG. 3. Twist-3 DAs $g^{(v)}$ and $g^{(a)}$ predicted by hQCD. The uncertainty band is due to the variation of the quark mass and the fundamental scale for holographic QCD.

where $C_j^{3/2}$ are the Gegenbauer polynomials and the coefficients $a_j^{\parallel,\perp}(\mu)$ are related to the moments $\langle \xi_{\parallel,\perp}^n \rangle_{\mu}$ [36]. These moments and coefficients are determined at a starting scale $\mu = 1$ GeV and can then be evolved perturbatively to higher scales [35]. For mesons with definite G parity (equal mass quark antiquark), i.e., ϕ in our case, $a_1^{\parallel,\perp} = 0$ [37]. For the other two coefficients, we adopt $a_2^{\parallel} = 0.23 \pm 0.08$ and $a_2^{\perp} = 0.14 \pm 0.07$ from references [6,37]. In Fig. 2, we show the predictions of holographic QCD for twist-2 DAs compared with those obtained from QCDSR.

Figure 2 shows twist-2 DAs $\phi_{\parallel,\perp}(x,\mu = 1$ GeV) for the ϕ vector meson obtained using Eqs. (19) and (20) as compared to SR predictions as given by Eq. (23). The uncertainty band for holographic DAs are due to the uncertainties in quark mass and the fundamental AdS/QCD scale: $m_s = 0.40 \pm 0.15$ GeV and $\kappa = 0.54 \pm 0.02$ GeV. The error band in SR DAs are the result of the uncertainties in the Gegenbauer coefficients as given above.

The twist-3 DAs can also be obtained from the light-front wave function through the following expressions [25]

$$g_{\perp}^{(v)}(x) = \frac{N_c}{2\pi f_{\phi} m_{\phi}} \int db \mu J_1(\mu b) [m_s^2 - (x^2 + (1-x)^2 \nabla_b^2)] \times \frac{\Psi_T^{\phi}(x, \zeta)}{x^2(1-x)^2}, \quad (24)$$

$$\frac{dg_{\perp}^{(a)}(x)}{dx} = \frac{\sqrt{2} N_c}{\pi f_{\phi} m_{\phi}} \int db \mu J_1(\mu b) [(1-2x)m_s^2 - \nabla_b^2] \times \frac{\Psi_T^{\phi}(x, \zeta)}{x^2(1-x)^2}. \quad (25)$$

Figure 3 shows the twist-3 DAs for ϕ meson which are obtained from Eqs. (24) and (25). As is evident from the figures, the uncertainty due to m_s and κ , contrary to the case for $g^{(v)}$, is negligible for $g^{(a)}$. In the next section, we use the decay constants and DAs up to twist-3 to compute the transition form factors (TFFs) $B_s \rightarrow \phi$.

V. $B_s \rightarrow \phi$ TRANSITION FORM FACTORS

The seven $B_s \rightarrow \phi$ TFFs are defined as [38]

$$\begin{aligned} & \langle \phi(k, \varepsilon) | \bar{s} \gamma^{\mu} (1 - \gamma^5) b | B_s(p) \rangle \\ &= \frac{2iV(q^2)}{m_{B_s} + m_{\phi}} \epsilon^{\mu\nu\rho\sigma} \varepsilon_{\nu}^* k_{\rho} p_{\sigma} - 2m_{\phi} A_0(q^2) \frac{\varepsilon^* \cdot q}{q^2} q^{\mu} \\ & - (m_{B_s} + m_{\phi}) A_1(q^2) \left(\varepsilon^{\mu*} - \frac{\varepsilon^* \cdot q q^{\mu}}{q^2} \right) \\ & + A_2(q^2) \frac{\varepsilon^* \cdot q}{m_{B_s} + m_{\phi}} \left[(p+k)^{\mu} - \frac{m_{B_s}^2 - m_{\phi}^2}{q^2} q^{\mu} \right], \quad (26) \end{aligned}$$

TABLE II. Numerical values of the input parameters.

| | | | |
|---------------------|-----------|-----------|---------------------|
| m_{B_s} | 5.367 GeV | M_B | 8 GeV ² |
| α^{-1} | 127 | s_0 | 36 GeV ² |
| $ V_{tb} V_{ts}^* $ | 0.0407 | f_{B_s} | 0.224 GeV |
| τ_{B_s} | 1.512 ps | m_b | 4.8 GeV |

TABLE III. hQCD+ lattice predictions for the form factors. Lattice data are taken from [38]. The error bars for the holographic form factors are due to the variation in m_s and κ , as explained in the text.

| | V | A_0 | A_1 | A_2 | T_1 | T_2 | T_3 |
|-------------|------------------------|------------------------|-------------------------|------------------------|------------------------|------------------|-------------------------|
| F(0) (hQCD) | 0.26 ± 0.2 | 0.15 ± 0.03 | 0.19 ± 0.02 | 0.21 ± 0.01 | 0.21 ± 0.03 | 0.22 ± 0.01 | 0.16 ± 0.01 |
| F(0) (SR) | 0.33 ± 0.01 | 0.27 ± 0.01 | 0.26 ± 0.01 | 0.26 ± 0.01 | 0.27 ± 0.01 | 0.28 ± 0.01 | 0.18 ± 0.01 |
| a (hQCD) | 1.66 ± 0.06 | $2.21^{+0.18}_{-0.15}$ | $0.85^{+0.08}_{-0.07}$ | 1.41 ± 0.22 | $1.76^{+0.20}_{-0.16}$ | 0.51 ± 0.01 | $0.55^{+0.32}_{-0.42}$ |
| a (SR) | 1.50 ± 0.01 | 1.26 ± 0.03 | 0.24 ± 0.02 | $1.35^{+0.31}_{-0.12}$ | 1.51 ± 0.02 | 0.046 ± 0.01 | 0.73 ± 0.19 |
| b (hQCD) | $0.60^{+0.08}_{-0.07}$ | $1.26^{+0.24}_{-0.19}$ | $-0.23^{+0.07}_{-0.06}$ | $0.51^{+0.66}_{-0.13}$ | $0.74^{+0.25}_{-0.20}$ | -0.63 ± 0.05 | $-0.98^{+0.44}_{-0.55}$ |
| b (SR) | 0.45 ± 0.01 | -0.013 ± 0.048 | -0.86 ± 0.03 | $0.62^{+0.85}_{-0.39}$ | 0.48 ± 0.03 | -1.08 ± 0.03 | $-0.65^{+0.23}_{-0.19}$ |

$$\begin{aligned} & q_{\nu} \langle \phi(k, \varepsilon) | \bar{s} \sigma^{\mu\nu} (1 + \gamma^5) b | B_s(p) \rangle \\ &= 2T_1(q^2) \epsilon^{\mu\nu\rho\sigma} \varepsilon_{\nu}^* p_{\rho} k_{\sigma} \\ & + iT_2(q^2) [(\varepsilon^* \cdot q)(p+k)_{\mu} - \varepsilon_{\mu}^* (m_{B_s}^2 - m_{\phi}^2)] \\ & + iT_3(q^2) (\varepsilon^* \cdot q) \left[\frac{q^2}{m_{B_s}^2 - m_{\phi}^2} (p+k)_{\mu} - q_{\mu} \right], \quad (27) \end{aligned}$$

where $q = p - k$ is the 4-momentum transfer and ε is the polarization 4-vector of the ϕ . At low-to-intermediate values of q^2 , these TFFs can be computed using QCD light-cone sum rules (LCSR) [11,39,40]. Here we use the LCSR expressions from Ref. [24] which are modified for the $B_s \rightarrow \phi$ decay channel. Table II shows the numerical values of the input parameters used in our predictions of the TFFs and the decay rate. The form factors, computed via LCSR, are valid at low to intermediate q^2 . The extrapolation to high q^2 is performed via a two-parameter fit of the following form

$$F(q^2) = \frac{F(0)}{1 - a(q^2/m_{B_s}^2) + b(q^4/m_{B_s}^4)} \quad (28)$$

to the LCSR predictions as well as form factor values obtained by lattice QCD which are available at high q^2 . The results for the above fit are given in Table III. We note that hQCD predicts lower values of the form factors at $q^2 = 0$ compared to those obtained from SR.

Figure 4 shows the comparison between hQCD and SR predictions including the lattice data points at high q^2 for the form factors. The shaded bands in these figures represent the uncertainty due to the error band in the DAs. Note that there are additional uncertainties in the form factors inherent in the LCSR method (uncertainty in the Borel parameter, continuum threshold and other input parameters). Since our goal in this paper is to discriminate between the hQCD and SR models and that the inherent LCSR uncertainties are the same in both models, we do not include them here.

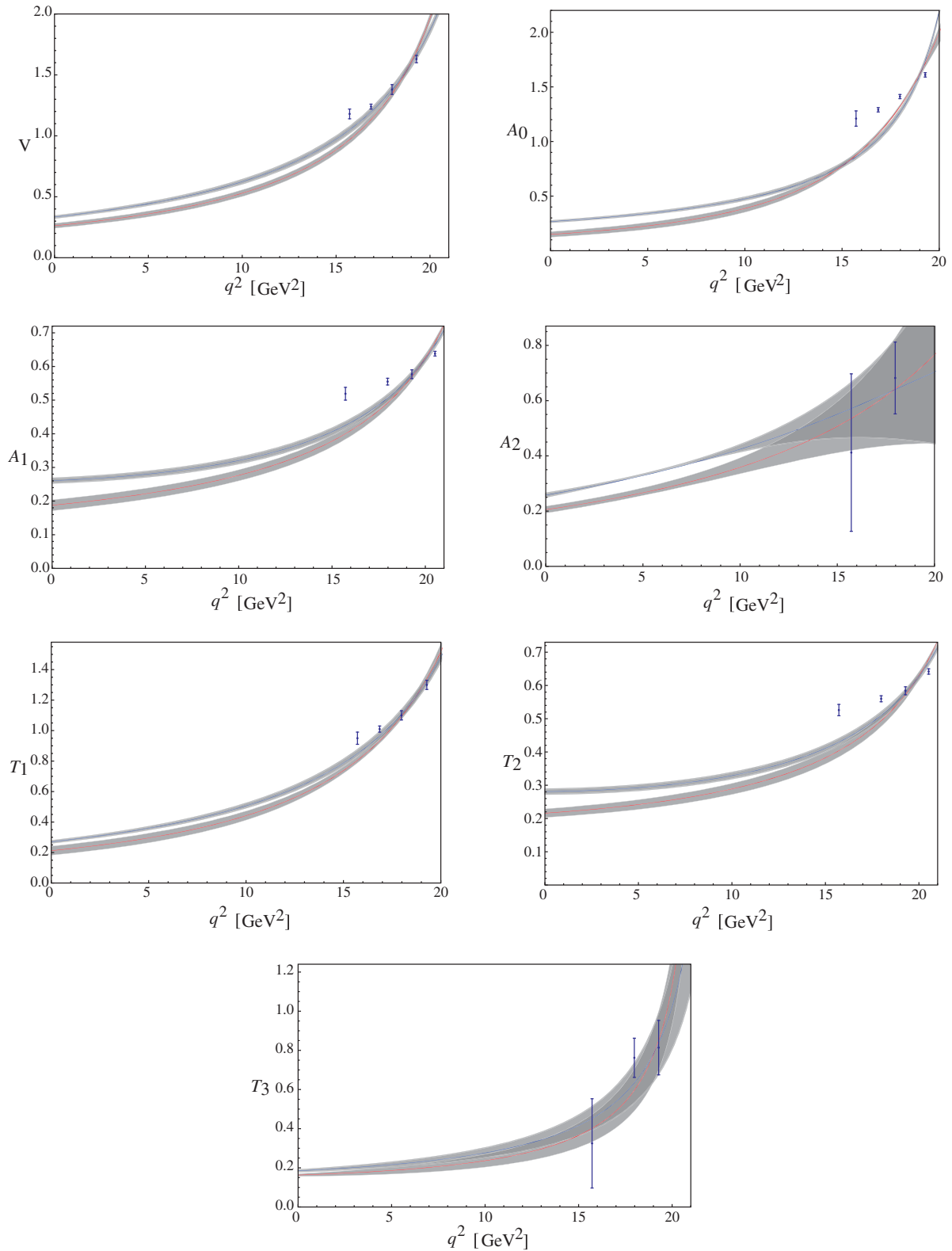


FIG. 4. hQCD (red curves) and QCDSR (blue curves) predictions for the $B_s \rightarrow \phi$ TFFs. The two-parameter fits with the available lattice data are used for the plots. The shaded bands represent the uncertainty in the predicted form factors due to uncertainty bands in DAs and variation in quark masses. Lattice data points (shown on plots) are taken from [38].

VI. DIFFERENTIAL DECAY RATE

The differential branching ratio for $B_s \rightarrow \phi\mu^+\mu^-$ is given by the following expression [39]:

$$\begin{aligned} \frac{d\mathcal{B}}{dq^2} = & \tau_{B_s} \frac{G_F^2 \alpha^2 |V_{tb} V_{ts}^*|^2 \sqrt{\lambda} v}{2^{11} \pi^5 3m_{B_s}} \left((2m_\mu^2 + m_{B_s}^2 s) \left[16(|A|^2 + |C|^2) m_{B_s}^4 \lambda + 2(|B_1|^2 + |D_1|^2) \right. \right. \\ & \times \frac{\lambda + 12rs}{rs} + 2(|B_2|^2 + |D_2|^2) \frac{m_{B_s}^4 \lambda^2}{rs} - 4[\Re(B_1 B_2^*) + \Re(D_1 D_2^*)] \frac{m_{B_s}^2 \lambda}{rs} (1 - r - s) \left. \right] \\ & + 6m_\mu^2 \left[-16|C|^2 m_{B_s}^4 \lambda + 4\Re(D_1 D_3^*) \frac{m_{B_s}^2 \lambda}{r} - 4\Re(D_2 D_3^*) \frac{m_{B_s}^4 (1-r)\lambda}{r} + 2|D_3|^2 \frac{m_{B_s}^4 s \lambda}{r} \right. \\ & \left. \left. - 4\Re(D_1 D_2^*) \frac{m_{B_s}^2 \lambda}{r} - 24|D_1|^2 + 2|D_2|^2 \frac{m_{B_s}^4 \lambda}{r} (2 + 2r - s) \right] \right) \end{aligned}$$

where $\lambda = 1 + r^2 + s^2 - 2r - 2s - 2rs$, with $r = m_\phi^2/m_{B_s}^2$ and $s = q^2/m_{B_s}^2$. The final muon has mass m_μ and velocity $v = \sqrt{1 - 4m_\mu^2/q^2}$. The differential branching fraction depends on the following combinations of form factors:

$$A = C_9^{\text{eff}} \left(\frac{V}{m_{B_s} + m_\phi} \right) + 4C_7 \frac{m_b}{q^2} T_1, \quad (29)$$

$$B_1 = C_9^{\text{eff}} (m_{B_s} + m_\phi) A_1 + 4C_7 \frac{m_b}{q^2} (m_{B_s}^2 - m_\phi^2) T_2, \quad (30)$$

$$B_2 = C_9^{\text{eff}} \left(\frac{A_2}{m_{B_s} + m_\phi} \right) + 4C_7 \frac{m_b}{q^2} \left(T_2 + \frac{q^2}{m_{B_s}^2 - m_\phi^2} T_3 \right), \quad (31)$$

$$C = C_{10} \left(\frac{V}{m_{B_s} + m_\phi} \right), \quad (32)$$

$$D_1 = C_{10} (m_{B_s} + m_\phi) A_1, \quad (33)$$

$$D_2 = C_{10} \left(\frac{A_2}{m_{B_s} + m_\phi} \right), \quad (34)$$

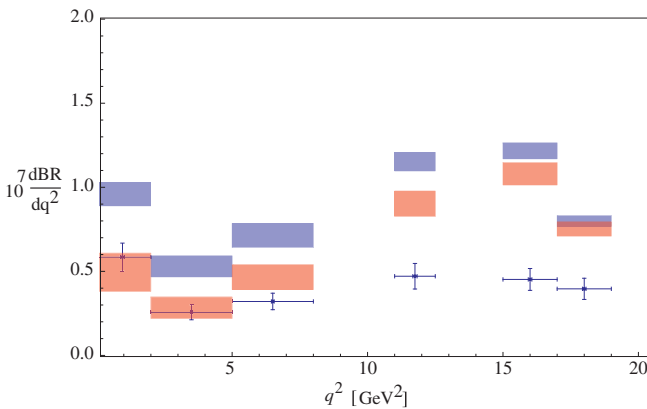


FIG. 5. The differential branching ratio for $B_s \rightarrow \phi\mu^+\mu^-$ as predicted by hQCD (red rectangles) and SR (blue rectangles). The uncertainty widths are due to the form factors. The experimental data points are measured by LHCb [5].

and

$$D_3 = -C_{10} \frac{2m_\phi}{q^2} (A_3 - A_0), \quad (35)$$

where

$$A_3 = A_0 - \frac{q^2}{2m_\phi m_{B_s} + m_\phi}. \quad (36)$$

As for the SM Wilson coefficients C_7 , $C_9^{\text{eff}} = C_9 + Y(q^2)$ and C_{10} appearing in the above equations, are given in Ref. [41]. Figure 5 shows the hQCD and QCDSR predictions for $B_s \rightarrow \phi\mu^+\mu^-$ differential branching ratio compared with the available experimental data from LHCb [5]. We observe that at low momentum transfer where the form factors are most sensitive to DAs through LCSR, hQCD produces better agreement with the data. The bin-by-bin numerical predictions are given in Table IV.

Using our hQCD predictions for $B \rightarrow K^*\mu^+\mu^-$ decay [22], we can consider the ratio

$$R_{K^*\phi}[q_1, q_2] = \frac{d\text{BR}(B^0 \rightarrow K^{*0}\mu^+\mu^-)/dq^2|_{[q_1, q_2]}}{d\text{BR}(B_s \rightarrow \phi\mu^+\mu^-)/dq^2|_{[q_1, q_2]}}, \quad (37)$$

by using the differential branching ratios integrated over range $[q_1, q_2]$. Figure 6 shows a graphical comparison of

TABLE IV. Bin-by-bin hQCD and QCDSR predictions for the $B_s \rightarrow \phi\mu^+\mu^-$ branching ratio compared with the experimental data from LHCb [5].

| q^2 (GeV) | $10^7 \langle \mathcal{BR}^{\text{hQCD}} \rangle$ | $10^7 \langle \mathcal{BR}^{\text{QCDSR}} \rangle$ | $10^7 \langle \mathcal{BR}^{\text{experiment}} \rangle$ |
|-------------|---|--|---|
| 0.1–2.0 | $0.49^{+0.12}_{-0.11}$ | 0.96 ± 0.07 | 0.59 ± 0.07 |
| 2–5 | $0.29^{+0.05}_{-0.07}$ | $0.54^{+0.05}_{-0.07}$ | 0.26 ± 0.04 |
| 5–8 | $0.48^{+0.06}_{-0.08}$ | $0.73^{+0.06}_{-0.09}$ | 0.32 ± 0.04 |
| 11.0–12.5 | $0.91^{+0.07}_{-0.08}$ | 1.15 ± 0.06 | 0.47 ± 0.07 |
| 15–17 | $1.08^{+0.07}_{-0.06}$ | 1.21 ± 0.05 | $0.45^{+0.06}_{-0.05}$ |
| 17.0–19.0 | 0.75 ± 0.04 | $0.80^{+0.04}_{-0.03}$ | $0.40^{+0.06}_{-0.05}$ |

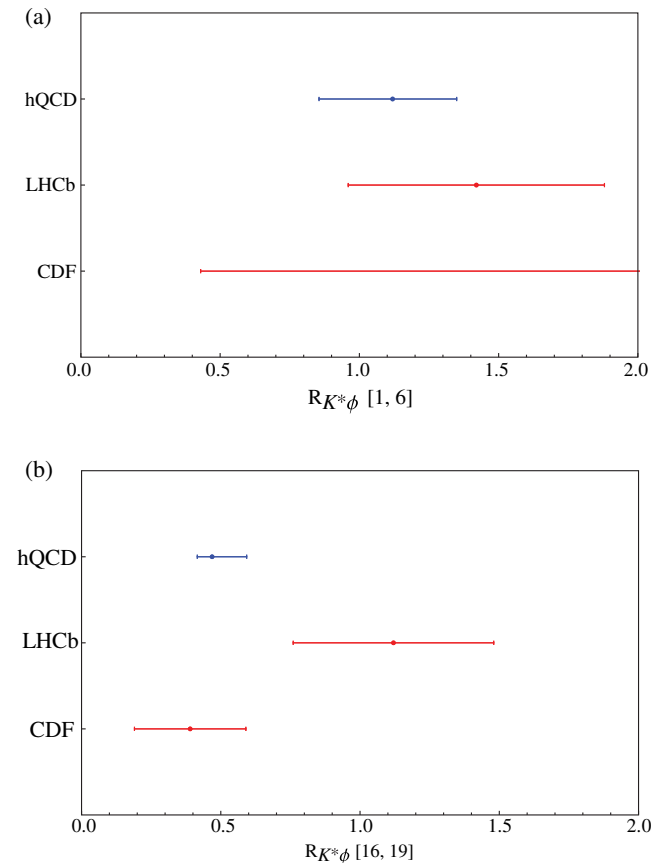


FIG. 6. hQCD prediction for $R_{K^*\phi}$ at low and high q^2 ranges as compared with the experimental data from LHCb [8,9] and CDF [42].

our predictions for $R_{K^*\phi}$ to the experimental data of LHCb [8,9] and CDF [42] at low and high q^2 range. It is encouraging that in low q^2 , the hQCD prediction agrees, within the error bars, with both LHCb and CDF results. Again, one should note that LCSR method for the evaluation of the transition form factors are expected to be more reliable at low q^2 . On the other hand, at high q^2 , our prediction only agrees with the CDF datum.

VII. CONCLUSION

We have calculated the $B_s \rightarrow \phi$ transition form factors using ϕ meson holographic DAs. Our prediction for the $B_s \rightarrow \phi \mu^+ \mu^-$ differential branching ratio is in better agreement with the latest LHCb data than the prediction generated using QCDSR DAs. In addition, we found that the hQCD prediction for $R_{K^*\phi}$ is in excellent agreement with both LHCb and CDF data at low q^2 . We conclude that it is important to have a better understanding of non-perturbative effects in rare $B_{(s)}$ decays.

ACKNOWLEDGMENTS

M.A and R.S are supported by Individual Discovery Grants from the Natural Science and Engineering Research Council of Canada (NSERC): SAPIN-2017-00033 and SAPIN-2017-00031 respectively. We would like to thank Idriss Amadou Ali for his contribution in the numerical computations of this work.

-
- [1] T. Aaltonen *et al.* (CDF Collaboration), *Phys. Rev. Lett.* **106**, 161801 (2011).
 [2] T. Aaltonen *et al.* (CDF Collaboration), *Phys. Rev. Lett.* **107**, 201802 (2011).
 [3] R. Aaij *et al.* (LHCb Collaboration), *J. High Energy Phys.* **07** (2013) 084.
 [4] W. Altmannshofer and D. M. Straub, *Eur. Phys. J. C* **75**, 382 (2015).
 [5] R. Aaij *et al.* (LHCb Collaboration), *J. High Energy Phys.* **09** (2015) 179.
 [6] A. Bharucha, D. M. Straub, and R. Zwicky, *J. High Energy Phys.* **08** (2016) 098.
 [7] C. Q. Geng and C. C. Liu, *J. Phys. G* **29**, 1103 (2003).
 [8] R. Aaij *et al.* (LHCb Collaboration), *J. High Energy Phys.* **08** (2013) 131.
 [9] R. Aaij *et al.* (LHCb Collaboration), *J. High Energy Phys.* **06** (2014) 133.
 [10] R. Aaij *et al.* (LHCb Collaboration), *J. High Energy Phys.* **10** (2014) 064.
 [11] A. Ali, V. M. Braun, and H. Simma, *Z. Phys. C* **63**, 437 (1994).
 [12] M. Ahmady, R. Sandapen, and N. Sharma, *Phys. Rev. D* **94**, 074018 (2016).
 [13] G. F. de Teramond and S. J. Brodsky, *Phys. Rev. Lett.* **94**, 201601 (2005).
 [14] S. J. Brodsky and G. F. de Teramond, *Phys. Rev. Lett.* **96**, 201601 (2006).
 [15] G. F. de Teramond and S. J. Brodsky, *Phys. Rev. Lett.* **102**, 081601 (2009).
 [16] S. J. Brodsky, G. F. de Teramond, H. G. Dosch, and J. Erlich, *Phys. Rep.* **584**, 1 (2015).
 [17] V. de Alfaro, S. Fubini, and G. Furlan, *Nuovo Cimento A* **34**, 569 (1976).
 [18] S. J. Brodsky, G. F. de Teramond, and H. G. Dosch, *Nuovo Cimento Soc. Ital. Fis.* **036C**, 265 (2013).
 [19] S. J. Brodsky and G. F. de Teramond, in *Search for the "Totally Unexpected" in the LHC Era*, AdS/CFT and Light-Front QCD Vol. 45 (World Scientific, Singapore, 2009), pp. 139–183.

- [20] J.R. Forshaw and R. Sandapen, *Phys. Rev. Lett.* **109**, 081601 (2012).
- [21] M. Ahmady, A. Leger, Z. McIntyre, A. Morrison, and R. Sandapen, *Phys. Rev. D* **98**, 053002 (2018).
- [22] M. Ahmady, D. Hatfield, S. Lord, and R. Sandapen, *Phys. Rev. D* **92**, 114028 (2015).
- [23] M.R. Ahmady, S. Lord, and R. Sandapen, *Phys. Rev. D* **90**, 074010 (2014).
- [24] M. Ahmady, R. Campbell, S. Lord, and R. Sandapen, *Phys. Rev. D* **89**, 074021 (2014).
- [25] M. Ahmady and R. Sandapen, *Phys. Rev. D* **88**, 014042 (2013).
- [26] M. Ahmady and R. Sandapen, *Phys. Rev. D* **87**, 054013 (2013).
- [27] P. Ball, V.M. Braun, Y. Koike, and K. Tanaka, *Nucl. Phys.* **B529**, 323 (1998).
- [28] M. Tanabashi *et al.* (Particle Data Group), *Phys. Rev. D* **98**, 030001 (2018).
- [29] A. Anastasi *et al.* (KLOE-2 Collaboration), *Phys. Lett. B* **767**, 485 (2017).
- [30] P. Ball and V.M. Braun, *Phys. Rev. D* **58**, 094016 (1998).
- [31] D. Becirevic, V. Lubicz, F. Mescia, and C. Tarantino, *J. High Energy Phys.* 05 (2003) 007.
- [32] V.M. Braun, T. Burch, C. Gatteringer, M. Gockeler, G. Lacagnina, S. Schaefer, and A. Schafer, *Phys. Rev. D* **68**, 054501 (2003).
- [33] K. Jansen, C. McNeile, C. Michael, and C. Urbach (ETM Collaboration), *Phys. Rev. D* **80**, 054510 (2009).
- [34] F. Gao, L. Chang, Y.-X. Liu, C.D. Roberts, and S.M. Schmidt, *Phys. Rev. D* **90**, 014011 (2014).
- [35] P. Ball, V.M. Braun, and A. Lenz, *J. High Energy Phys.* 08 (2007) 090.
- [36] H.-M. Choi and C.-R. Ji, *Phys. Rev. D* **75**, 034019 (2007).
- [37] P. Ball and G.W. Jones, *J. High Energy Phys.* 03 (2007) 069.
- [38] R.R. Horgan, Z. Liu, S. Meinel, and M. Wingate, *Phys. Rev. D* **89**, 094501 (2014).
- [39] T.M. Aliev, A. Ozpineci, and M. Savci, *Phys. Rev. D* **56**, 4260 (1997).
- [40] P. Ball and R. Zwicky, *Phys. Rev. D* **71**, 014029 (2005).
- [41] W. Altmannshofer, P. Ball, A. Bharucha, A. J. Buras, D. M. Straub, and M. Wick, *J. High Energy Phys.* 01 (2009) 019.
- [42] CDF Public Note 10894 (2012).